Bulletin of the Seismological Society of America, Vol. 105, No. 4, pp. 2117–2127, August 2015, doi: 10.1785/0120140247

Optimal Interpolation of Spatially Discretized Geodetic Data

by Zheng-Kang Shen,* Min Wang, Yuehua Zeng, and Fan Wang

Abstract We present an algorithm to calculate horizontal strains (or strain rates) through interpolation of geodetically derived displacements (or velocities). This is an underdetermined inverse problem to derive smoothly distributed strains (or strain rates) using spatially discretized geodetic observations. *A priori* information, in the form of weighted smoothing, is critical to facilitate the solution. At a given site, the horizontal displacement (or velocity) field in its vicinity is approximated by a bilinear function and represented by rigid block translation, rotation, and strains (or their rates). The weighted displacement (or velocity) data in the neighborhood are used to estimate the field parameters through a least-squares inversion procedure. Optimal weightings are prescribed for the neighboring data, based on their distances to the interpolation site and their spatial coverage. Nonelastic strains resulted from surface fault rupture and creep may also be excluded from the solution. We apply this method to the Southern California Earthquake Center Crustal Motion Map version 4.0 velocity field and derive the strain-rate field in southern California. Our result shows that (1) distance-dependent weighting can be optimally achieved by employing either a Gaussian or quadratic decay function, with the former offering a slightly sharper result than the latter. (2) Spatially dependent weighting is important to improve the interpolation, and can be done by invoking either an azimuthal weighting or a Voronoi cell areal weighting function. (3) The strain-rate pattern in southern California is dominated by dextral shear of the San Andreas fault (SAF) system, and the secondary faults surrounding the Big Bend of the SAF strike at oblique angles with respect to the maximum shear direction, suggesting that tectonic deformation field on and off the SAF is dominated by mechanic processes of the SAF.

Introduction

Geophysical studies frequently require estimating crustal strains or strain rates from discrete geodetic measurements. The data can be angle changes between stations, baseline line length changes, and/or station displacements for horizontal strain estimates. Strain rates are estimated when the changes are divided by the time span during which the changes take place. In the following text, we will use the term strain, with the knowledge that this word is interchangeable with the term strain rate, as the latter is merely a time derivative of the former, and all the methods and techniques discussed here can be equally applied.

A variety of methods have been developed to model strains using geodetic data. One group of such methods divides a region under investigation into subnetworks, and uses the data within each subnetwork to estimate mean strains inside the subnetwork (e.g., Frank, 1966; Prescott, 1976; Brunner *et al.*, 1981). However, these methods usually yield discontinuous strain estimates at the subnetwork boundaries. Such discontinuities are artifacts caused by abrupt changes of data input for model evaluation across the subnetwork boundaries.

To tackle the aforementioned problem, a school of methods were developed using a continuous modeling approach (e.g., El-Fiky *et al.*, 1997; El-Fiky and Kato, 1999). These methods usually estimate the global variance and covariance of the displacements first, and then use the variance and covariance as a spatial weighting function to interpolate discrete displacements into a continuous field. The strains are derived as spatial derivatives of the continuous displacement field. These methods basically adopt the concepts of geostatistics (Matheron, 1970; Wackernagel, 1995), and one of such applications is the Kriging technique (Srivastava and Isaaks, 1989), commonly used for optimal interpolation of a discrete scalar field. These methods provide better interpolation of the displacement field than the early subnetwork method, but they are valid only with the assumption that the deformation field is homogeneous and isotropic. A homogeneous field means that it has a constant mean and its autocovariances depend only on the distance between points. The field is isotropic if the autocovariances are invariant under rotation. Unfortunately, these two conditions are often not met in real

*Also at Department of Earth, Planetary, and Space Sciences, University of California, Los Angeles, California 90095-1567.

world crustal deformation. A simple example is for a velocity field caused by strike-slip dislocation across a vertical fault beneath a locking depth; the mean surface velocity field under the circumstance would change across the fault boundary, and the autocovariances would be a function of the strike direction of the fault.

Another approach of interpolating the displacement field is to fit it by a spline function (e.g., Sandwell, 1987; Haines and Holt, 1993). Methods developed under such an algorithm have no assumption of homogeneity and isotropy for the displacement field. The algorithm usually predivides the region into a grid, and fit the data within the grid using spline functions. If the degree of spline function is predetermined, spatial resolution for the grid is then fixed (e.g., Holt *et al.*, 2000; Kreemer *et al.*, 2003). An alternative approach is to allow variation of the degree of spline function (or degree of tension), which is determined by users based on the goodness of data fitting (Mitášová and Mitáš, 1993; Wessel and Bercovici, 1998; Wessel and Becker, 2008). This approach is more flexible than the previous one and may provide a reasonable fitting to the data globally. However, if the spatial distribution of the data is heterogeneous it may not provide a good representation of the regional deformation field.

All of the methods mentioned above are based primarily on geometric information only. Another approach of the problem is to combine geometric information with physics-based models, such as incorporating information on fault location and faulting style and earthquake focal mechanism (e.g., Kreemer *et al.*, 2014), and utilizing dislocation-induced deformation in continuum media for model constraints (e.g., Noda and Matsu'ura, 2010). Strain-rate derivation and result comparison have been a focus at a couple of Earthscope and Southern California Earthquake Center (SCEC) meetings or workshops in recent years, variations of models and results based on the algorithms mentioned above were presented (e.g., Hearn *et al.*, 2010), and the debate about algorithms of strain-rate estimation continues. In this study, we focus on a method of geometric inversion without invoking any physics model, except for one application excluding shallow fault rupture or creeping effects from the strain inversion. A previous version of the algorithm was applied to California strain-rate estimation and the result was provided to the exercise of strain-rate comparison organized by SCEC, but this update has incorporated significant advancements over the previous version on spatial data weighting and resolution (for the computer code and an application example, see Data and Resources).

Method

Shen *et al.* (1996) introduced an algorithm to model strains as continuous functions using a modified least-squares method. This algorithm is iterated over a 2D space with arbitrarily small increments to warrant solution continuity. At each interpolation coordinate R, the horizontal velocity field is expanded to its first-order derivatives, that is, to be represented by a model of rigid block motion (translation and rotation) and a uniform strain field. The displacement data are then linked to the deformation parameters by a linear relationship:

$$\mathbf{d} = A\,\mathbf{m} + \boldsymbol{\epsilon}, \tag{1}$$

in which $\mathbf{d}$ is the data vector, $\mathbf{m}$ is the vector for the unknowns of translation, rotation, and strain, A is the partial derivative matrix, and $\boldsymbol{\epsilon}$ is the error vector. For the case of horizontal strain only, $\mathbf{m} = (U_x\ U_y\ \omega\ \tau_{xx}\ \tau_{xy}\ \tau_{yy})^T$ in a Cartesian coordinate system, U_x and U_y are the translation components in x and y directions, respectively, ω is the rotation, and τ_{xx}, τ_{xy}, and τ_{yy} are the horizontal strain components respectively. Equation (1) can also be written as

$$\begin{bmatrix} Vx_1 \\ Vy_1 \\ Vx_2 \\ Vy_2 \\ \cdots \\ Vx_n \\ Vy_n \end{bmatrix} = \begin{bmatrix} 1 & 0 & \Delta y_1 & \Delta x_1 & \Delta y_1 & 0 \\ 0 & 1 & -\Delta x_1 & 0 & \Delta x_1 & \Delta y_1 \\ 1 & 0 & \Delta y_2 & \Delta x_2 & \Delta y_2 & 0 \\ 0 & 1 & -\Delta x_2 & 0 & \Delta x_2 & \Delta y_2 \\ \cdots & \cdots & \cdots & \cdots & \cdots & \cdots \\ 1 & 0 & \Delta y_n & \Delta x_n & \Delta y_n & 0 \\ 0 & 1 & -\Delta x_n & 0 & \Delta x_n & \Delta y_n \end{bmatrix} \begin{bmatrix} U_x \\ U_y \\ \omega \\ \tau_x \\ \tau_{xy} \\ \tau_y \end{bmatrix} + \begin{bmatrix} \varepsilon_{x1} \\ \varepsilon_{y1} \\ \varepsilon_{x2} \\ \varepsilon_{y2} \\ \cdots \\ \varepsilon_{xn} \\ \varepsilon_{yn} \end{bmatrix}, \tag{2}$$

in which Vx_i and Vy_i are the displacement components of the ith site at location r_i. Δx_i and Δy_i are the vector components of $\Delta R_i = r_i - R$. Let $\boldsymbol{\epsilon} \sim N(0, C)$, and C be the covariance matrix of the velocity data, a least-squares solution can be obtained in the form of

$$\mathbf{m} = (A^T C^{-1} A)^{-1} A^T C^{-1} \mathbf{d}. \tag{3}$$

Without modification of the data and/or their errors, the solution above would be for the mean strain field of the entire region. In Shen *et al.* (1996) and also in this study, the data are reweighted to give more weight to the sites located closer to site R. In Shen *et al.* (1996), a uniform Gaussian spatial weighting function was defined. In this study, we introduce the spatial weighting function in various forms, with their smoothing parameters optimally determined based on the *in situ* data strength.

We reconstruct the covariance matrix C by multiplying a weighting function to each of its diagonal terms C_i, and the weighting is given as $C_i \leftarrow C_i G_i^{-1}$. The weighting function $G_i = L_i \times Z_i$, in which L_i and Z_i are functions of distance and spatial coverage dependent, respectively. For distance-dependent weighting, L_i is assumed to be in the form of

$$L_i = \exp(-\Delta R_i^2/D^2) \qquad \text{or} \qquad (4a)$$

$$L_i = 1/(1 + \Delta R_i^2/D^2)\,, \qquad (4b)$$

in which a spatial smoothing parameter D is introduced. Both functions allow reduced weight of the data as distance increases. The difference between the two is that the Gaussian function reduces the weight at a faster pace with distance ΔR_i than that of the quadratic function. Depending on the data quality, the Gaussian function can offer a relatively finer resolution of the interpolation result if the data are clean and smooth. On the other hand, if the data are somewhat heterogeneous, the quadratic function is relatively more conservative and provides a more smoothed solution, especially for regions in which data are sparsely distributed. In addition, any data points with distance weighting function L less than a threshold value L_0 will be excluded. For $L_0 = 0.01$, it means a data selection radius of $R_0 = 2.15D$ for Gaussian weighting and $R_0 = 10D$ for quadratic weighting, respectively. Because the L weighting function is inversely multiplied to data variances, a 0.01 cutoff threshold on variance is equivalent to 0.1 weighting cutoff on data. That is, sites with less than 0.1 weights will be omitted.

Shen *et al.* (2007) introduced a method to optimally determine the smoothing distance D. At each evaluation coordinate, solutions with varying values of D were attempted, and a trade-off curve was acquired between W, the sum of the reweighting coefficients, and σ, the uncertainty of the strain-rate estimates (σ decreases as W increases, and vice versa). An optimal value of D would be selected in the middle of this trade-off curve. This approach indeed improved quality of the interpolation, but it still has a certain degree of arbitrariness because it is not certain precisely where along the curve the right spot is to pick the optimal value. In our current algorithm, we choose to leave the option of optimal value selection to the users. Let $W = \Sigma_i G_i$, the total reweighting coefficients of the data, and let W_t be the threshold of W. For a given W_t, the smoothing constant D is determined by $W(D) = W_t$. It should be noted that W is a function of the interpolation coordinate, therefore for the same W_t assigned, D varies spatially based on the *in situ* data strength; that is, the denser the local data array is, the smaller is D, and vice versa.

The Z_i function is important to compensate for the often unevenly distributed data points spatially and takes an option of two functional forms. One functional form measures the azimuth span of the site with respect to each of the data points selected in the previous step. As shown in Figure 1, at the interpolation site R, the azimuth span θ_i for data point i is measured between two strike directions of the $i-1$ and $i+1$ data points in its neighborhood, ranked in counterclockwise order. The azimuthal weighting function for the ith data point is then attributed as

$$Z_i = n\theta_i/4\pi, \qquad (5a)$$

in which n is the total number of data points selected.

An alternative way to assign spatially dependent weighting is through Voronoi cell (Fortune, 1992). The studied region is first meshed into Delaunay triangles based on the locations of the data points. These triangles are then further meshed into Voronoi cells by connecting the central division lines of the sides of Delaunay triangles, with one geodetic site located within each cell. The surface areas of these Voronoi cells are then used as reweighting coefficients

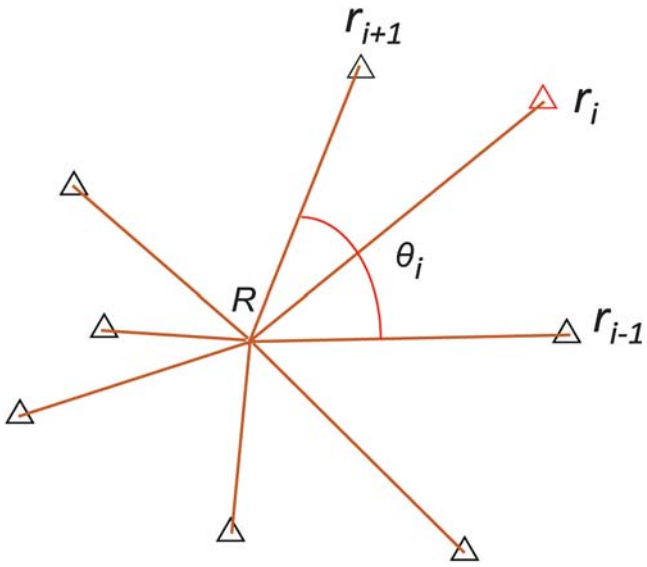

Figure 1. The azimuth span θ_i of geodetic data point r_i relative to interpolation site R. Triangles denote locations of geodetic data points near the interpolation site R.

$$Z_i = nS_i/\sum_{k=1}^{n} S_k, \qquad (5b)$$

in which S_i is the surface area of the Voronoi cell for the ith data point selected, and n is the total number of data points selected. Voronoi cell weighting was also used by Hsu *et al.* (2009); the major difference between their method and ours is that they imposed the weighting on data errors and we apply them on data variances. Comparing the azimuthal span and Voronoi cell weighting approaches, the former scales the weights based on the station azimuthal coverage only, whereas the latter measures the weights based on not only azimuthal but also radial range coverage of a station. Thus, they are virtually 1D versus 2D in their weighting factor determination.

Nonelastic deformation takes place if a fault is not locked interseismically in the brittle part of the crust due to surface rupture or creeping, causing discontinuous deformation across the fault. If one prefers to map elastic strain accumulation only, such nonelastic strain due to slip across a known fault needs to be removed. We therefore develop an algorithm to exclude the fault rupture or creeping effect, which takes place across a fault plane in the upper crust and results in little or no elastic strain accumulation. To do so, we set up a barrier along the rupture or creeping section of the fault, to screen out the data from the other side of the fault being used in interpolation calculation. At a given interpola-

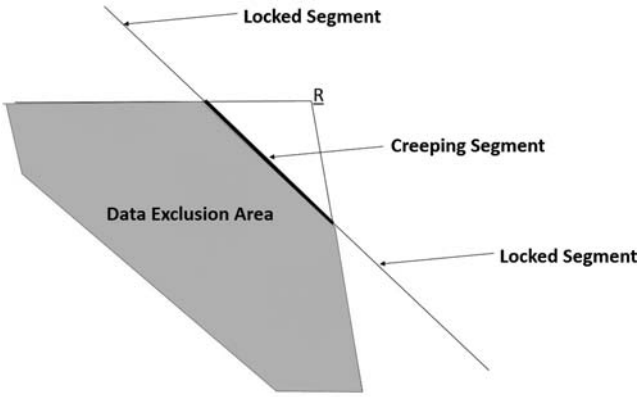

Figure 2. The data exclusion area near a creeping or ruptured fault. The thick black line denotes the creeping or rupture segment of a fault. *R* is the strain interpolation site. The gray area behind the creeping or rupture segment of the fault is the region where the geodetic data points are excluded from participating in the strain estimation.

tion coordinate, azimuthal directions of all the data points are evaluated. If a data point is hiding behind the fault barrier, or in other words, its azimuthal direction is within the azimuthal span of the barrier's two endpoints, that data point is removed from calculation. See Figure 2 for geometric illustration.

Method Application to Global Positioning System Velocity Field in Southern California

SCEC produced four versions of secular crustal motion velocity solution for southern California (Shen *et al.*, 1997, 2011). These solutions provided geodetic station secular velocities, coseismic offsets, and postseismic displacements, and were derived from a combination of geodetic data including electronic distance meter (EDM), very long baseline interferometry (VLBI), and Global Positioning System (GPS). The secular velocity field of the latest release, the SCEC Crustal Motion Map version 4.0 (CMM4) (Shen *et al.*, 2011) is shown in Figure 3, which includes 1092 station velocities covering a region of 32°–38° N, 114°–123° W for southern California, western Nevada, and northern Mexico (for the velocity dataset, see Data and Resources).

As described above, we use our code velocity interpolation for strain rate to interpolate the CMM4 velocity solution. To avoid redundant use of data, EDM and VLBI velocities tied to GPS at collocated sites are removed (Fig. 3). Four sets of solutions are produced using different combinations of data weighting functions, and the results are described below.

The first set of solutions is obtained employing the Gaussian function for distance weighting and Voronoi cell for areal weighting, respectively, and the net weighting threshold is set to be $W_t = 6$, 12, 24, and 48, respectively. The mesh of the Voronoi cells is shown in Figure 4. For the sites located at the vertices of the network exterior, their Voronoi cells often have strange shapes, and the cell areas are usually not adequate for areal weighting of the data. A different scheme is then employed to assign their areal weighting, in the form

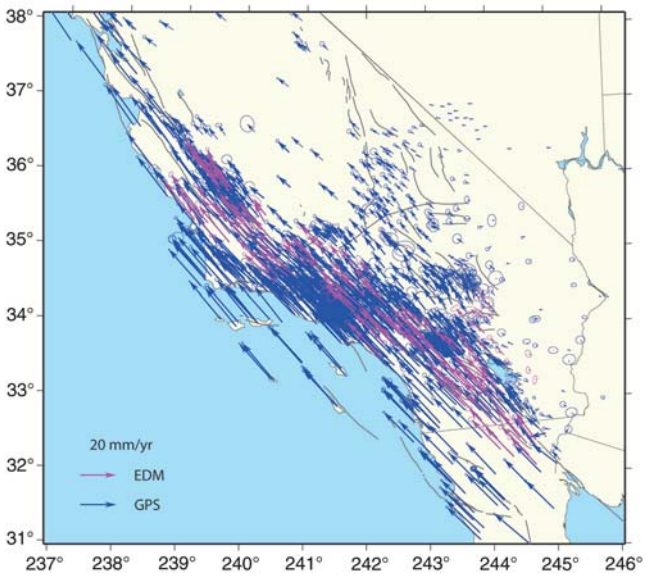

Figure 3. The secular velocity field of Southern California Earthquake Center (SCEC) Crustal Motion Map version 4.0 (CMM4). All the station velocities are referenced to the stable North America plate. Error ellipses represent 95% confidence.

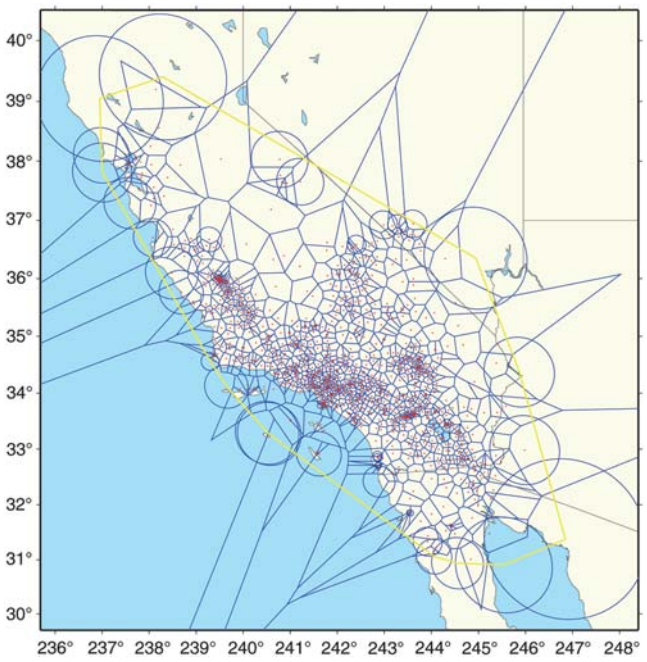

Figure 4. Voronoi cell meshing based on CMM4 network station distribution. For sites located at the vertices of the network exterior, their Voronoi cell areal weightings are replaced by circular areal weightings.

of πr_d^2, in which r_d is the mean of the distances between the interpolation site and six closest neighborhood data points. For some data points near the hull boundaries, their Voronoi cells may yield huge areas, resulting in unreasonably large weights. Their areal weightings are then reassigned to be πr_d^2 if their Voronoi cell areas are greater than $2\pi r_d^2$. Shapes of these circular areas for the vertices and some boundary

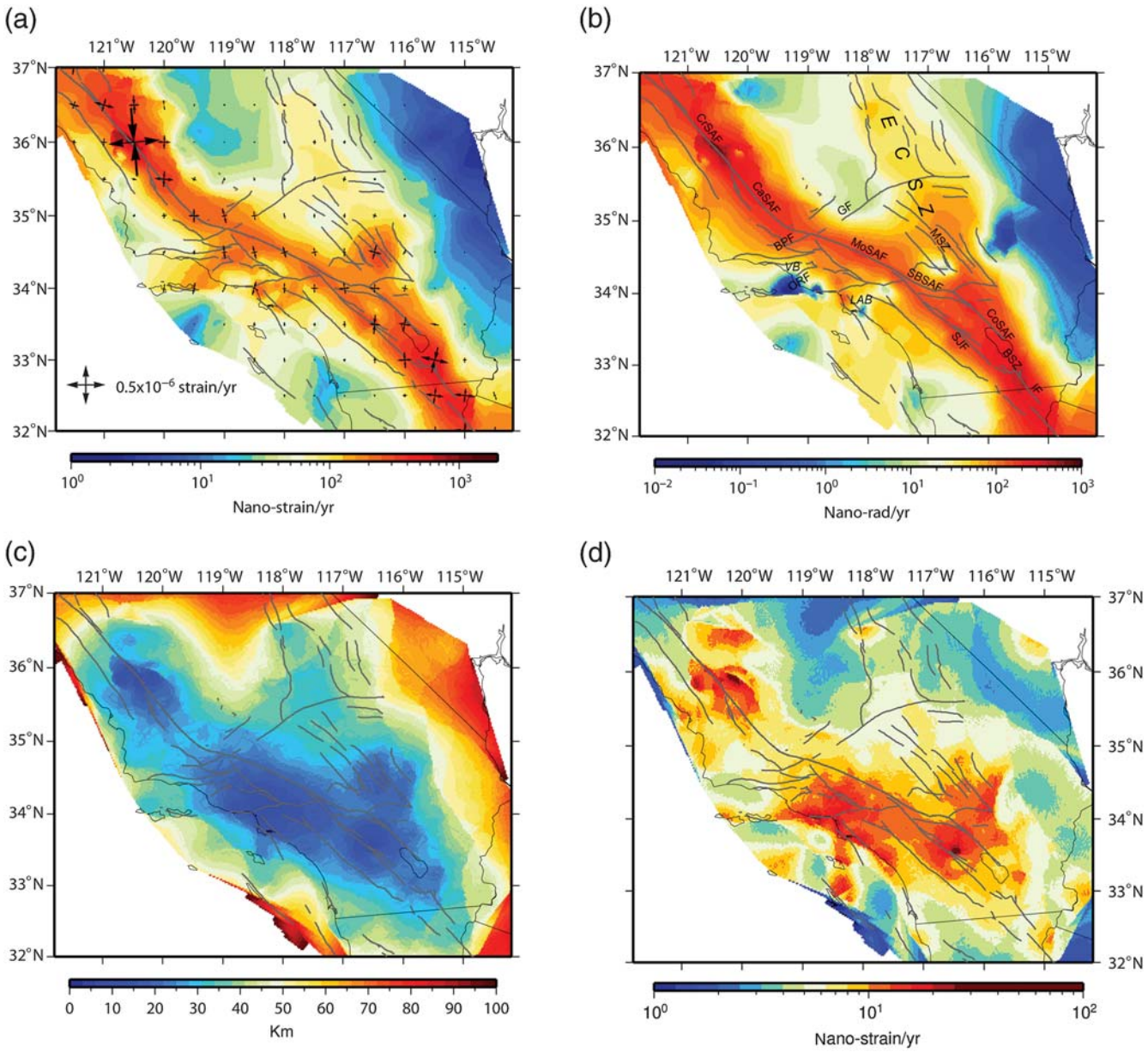

Figure 5. Interpolation result using Gaussian or Voronoi cell weighting functions with the net weighting threshold set as $W_t = 24$. (a) Second invariant of strain rates (background) and principal strain rates (arrow pairs). (b) Rotation rate. (c) Smoothing constant D. (d) Formal uncertainty of maximum shear-strain rate σ. CaSAF, Carrizo San Andreas fault; CoSAF, Coachella San Andreas fault; CrSAF, Creeping segment of San Andreas fault; MoSAF, Mojave San Andreas fault; SBSAF, San Bernardino San Andreas fault; SJF, San Jacinto fault; GF, Garlock fault; MSZ, Mojave Shear Zone; BPF, Big Pine fault; ORF, Oak Ridge fault; ECSZ, East California Shear Zone; LAB, Los Angeles basin; VB, Ventura basin.

sites are also plotted in Figure 4. Figure 5 shows the interpolation result obtained from one of the first set of solutions, with $W_t = 24$, including the principal strain rates, second invariant of horizontal strain rates, rotation rates, smoothing constant D, and shear-strain-rate uncertainty σ. The second invariant of horizontal strain rates is defined as

$$\tau_{2\text{inv}} = \sqrt{\tau_e^2 + \tau_n^2 + 2\tau_{en}^2}, \tag{6}$$

in which τ_e, τ_n, and τ_{en} are three strain-rate components in a north and east Cartesian coordinate system. To demonstrate the effect of selection of W_t, we plot the cases of $W_t = 6$, 12, and 48 in Figure 6, which shows clearly that as W_t increases, D also increases, and the strain rates become more smoothed, at the expense of less sharpness of the strain-rate pattern at certain regions with dense data population.

The second set of solutions is obtained using the Gaussian function for distance weighting and azimuthal span for spatial weighting, respectively. The weighting threshold W_t is chosen as 24, and the result of the second invariant of the strain rates is shown in Figure 7a. Comparing to the result obtained using Voronoi cell weighting (Fig. 5a for solution

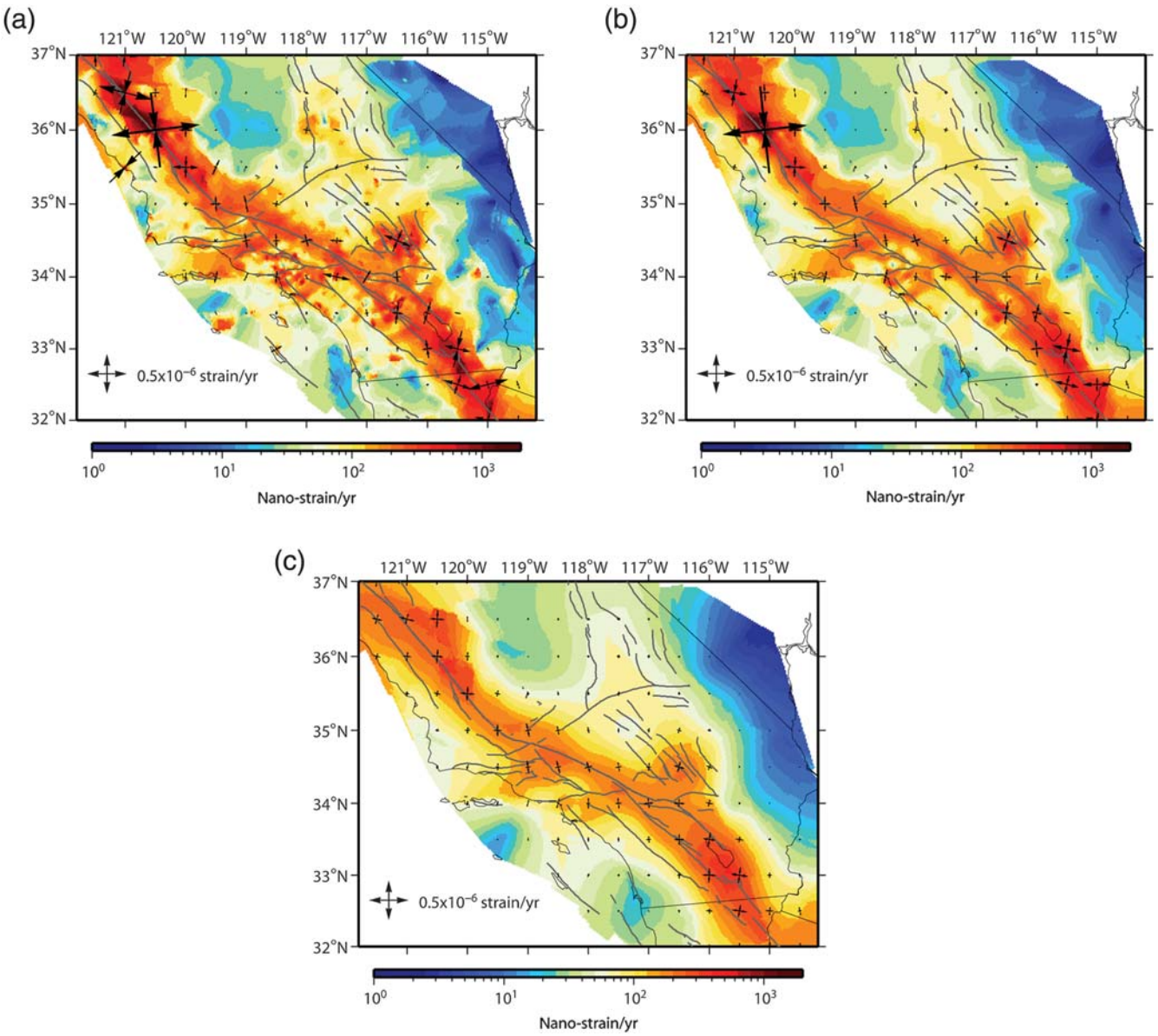

Figure 6. The second invariant of strain rates (background) and principal strain rates using Gaussian and Voronoi cell weighting functions with the net weighting thresholds set as $W_t = 6$, 12, and 48 for (a), (b), and (c), respectively.

obtained using the same weighting threshold), the one using azimuthal weighting is quite similar, except that the patterns at some areas are a bit less smoothed.

The third and fourth sets of solutions are obtained using quadratic functions for distance weighting, and Voronoi cell and azimuthal span for spatial weighting, respectively. To maintain the same sharpness of strain-rate pattern along the San Andreas fault (SAF), the total weighting threshold needs to be set as six for the quadratic or azimuthal span and three for the quadratic or Voronoi cell-weighting models respectively, and their results of second invariant of strain rates are shown in Figure 7b and 7c, respectively. Again the strain patterns are quite similar to the previous two models, but are not as smooth as that of the Gaussian or Voronoi cell model overall. Increased total weighting threshold results in more smoothed strain pattern, at the expense of less sharpness across the major fault zones.

A section of the SAF between Parkfield and San Juan Bautista in central California is known to creep almost freely throughout the brittle layer of the fault (Jolivet *et al.*, 2015). We implement an algorithm of creeping effect exclusion on this section of the fault, and calculate the strain rates using the Gaussian and Voronoi cell weighting with $W_t = 24$. The result is demonstrated in Figure 8, which shows that the high strain-rate concentration that appeared in previous figures around the section is gone. However, the high strain-rate concentrations around the two ends of the creeping section are still there reflecting relatively high strain rates around Parkfield and San Juan Bautista due to local partial creeping across the SAF.

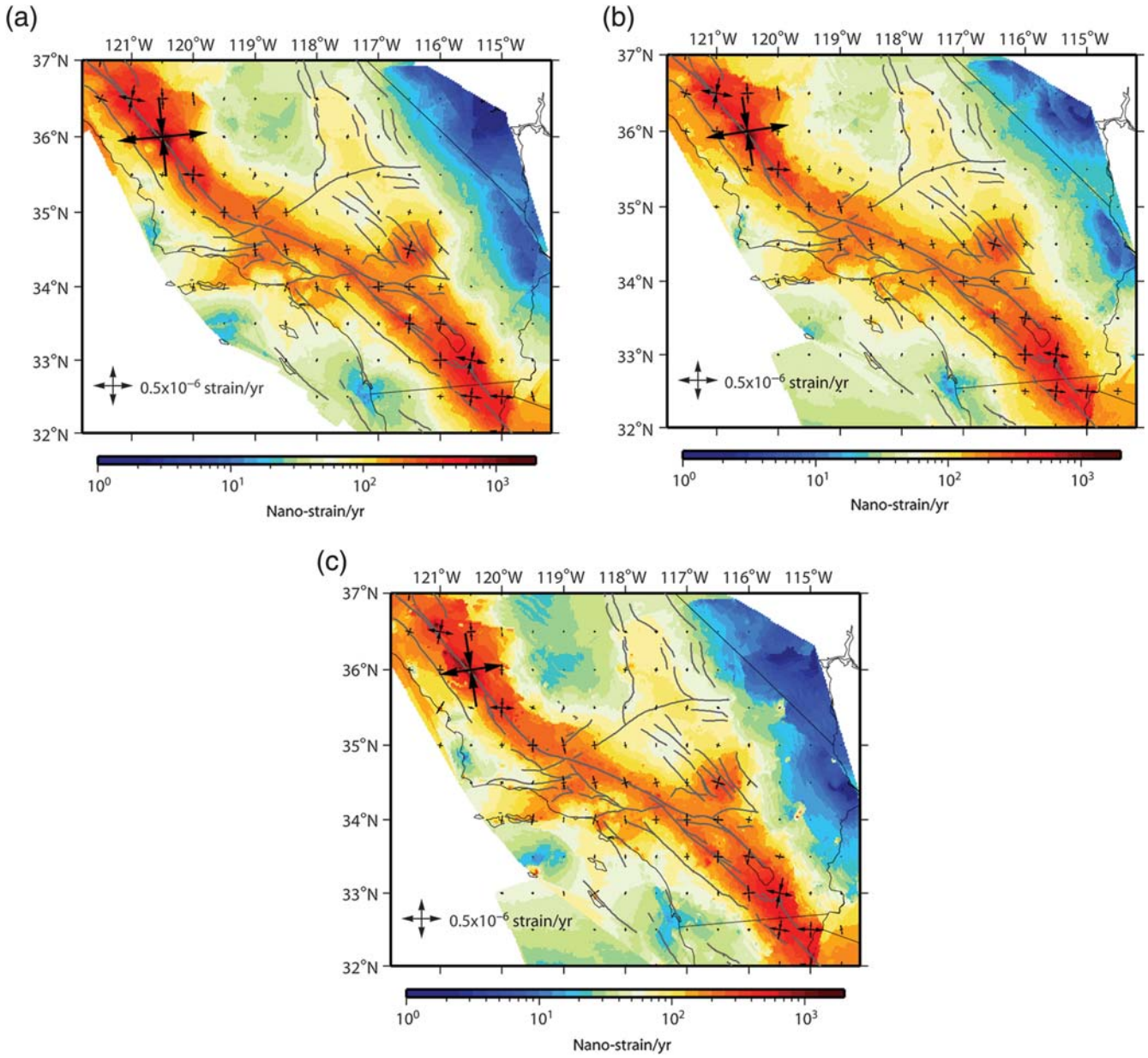

Figure 7. Interpolation result using different weighting functions. (a) Gaussian and azimuthal weighting and $W_t = 24$; (b) quadratic and azimuthal weighting and $W_t = 6$; (c) quadratic and voronoi cell weighting and $W_t = 3$. The background shows the second invariant of strain rates and the arrow pairs are the principal strain rates, respectively.

Discussions

Optimal Model Determination

In the section above, we described the common features and differences between different weighting schemes, and their abilities in interpolating regional GPS data for strain rate and rotation rate calculation with different weighting thresholds. However, with a given weighting scheme we need to find an optimal net weighting threshold W_t. One way to do so is through examination of differential strain-rate pattern of two strain-rate fields derived using different W_t.

Figure 9 shows three differential strain-rate fields of (a) $(W_t = 24) - (W_t = 48)$, (b) $(W_t = 12) - (W_t = 24)$, and (c) $(W_t = 6) - (W_t = 12)$ for the case of Gaussian and Voronoi cell weighting. The differential strain-rate field in Figure 9a is quite smooth with most of the strain-rate differences occurred along the SAF, particularly around the creeping section of the SAF and the Brawley Seismic Zone. Minor strain-rate differences can also be seen along faults in the Mojave Shear Zone and in the Transverse ranges. The pattern suggests that as W_t decreases from 48 to 24, the strain-rate model picks up more tectonic strain signals along the active faults. However, as W_t decreases from 24 to 12 (Fig. 9b), the differential strain-rate pattern starts to deteriorate somewhat comparing to that in Figure 9a, but still shows that most of the incremental strains are aligned with the known faults, indicating that additional

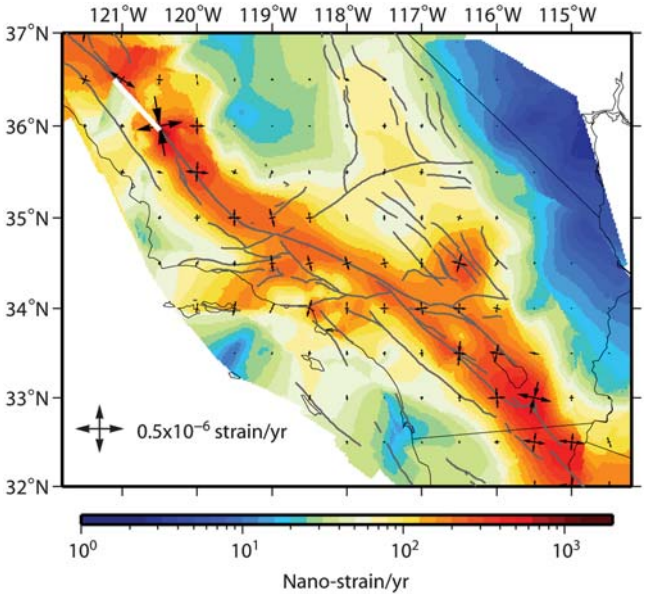

Figure 8. The same as the strain-rate result shown in Figure 5a except that the shallow creep effect associated with the SAF in central California is removed. The thick white line denotes the creeping section of the SAF.

tectonic strain signals are resolved. Noises are also shown up off-fault, and become quite significant at some places. For model of $W_t = 6$, the differential strain-rate pattern in Figure 9c deteriorates further comparing to the pattern in Figure 9b; although additional tectonic strains may still be detected along the creeping section of the SAF and the Brawley Seismic Zone, the noises start to take over the gain in the strain-rate signals along most other parts of the fault system. Balancing the trade-off between the resolution and robustness, we choose model $W_t = 24$ as the optimal model for characterization of the strain-rate field in southern California. Model $W_t = 12$ can also be an option if more resolution is preferred at the expense of slight increase of noise level.

We perform similar analysis for the solutions derived using the other three data weighting algorithms, and determine that the optimal solutions are $W_t = 24$ for Gaussian and azimuthal, $W_t = 6$ for quadratic and voronoi cell, and $W_t = 3$ for quadratic and azimuthal weightings, respectively. Depending on the preferences, room is still available for picking in the parameter range for the most optimal solutions, but its range is limited and centered on the optimal parameter we presented previously.

Assessment of Solution Uncertainties and Resolution

Several parameters are important in assessing the quality of strain-rate estimation. Figure 5d plots the formal uncertainty of shear-strain rate, which is deduced in the least-squares estimation. However, it is obvious from the figure that the formal uncertainty cannot be directly used, in a classic sense, to measure the quality of the result. As shown in the figure, contrary to intuition, the uncertainties are smaller in regions in which the data distributions are more sparse. This is because such uncertainties are measures of averaged strain rates, which are strongly affected by the degree of smoothing imposed on the data. As the degree of smoothing varies spatially, assessment of the spatial distribution of the smoothing range becomes a crucial part for the evaluation of real strain-rate uncertainties. Figure 5c shows the Gaussian smoothing coefficient D used in reweighting, which is a measure of the range of smoothing involved in the calculation. It can be regarded as a measure of the *in situ* data strength because it is reciprocally proportional to data density, and reflects spatial resolution of the result. For the assessment of quality of strain-rate interpolation result, it is more practical and useful to assess the relative resolution, as shown in Figure 5c, than to examine the formal uncertainty. This is because a strain-rate estimate at a given site, if averaged over a large area, cannot be taken as an accurate estimate for the site due to the lack of spatial constraints from data, no matter how small the formal uncertainty may become.

Tectonic Strains in Southern California

The strain-rate result we obtain clearly delineates the major faults in southern California, such as the SAF, San Jacinto fault (SJF), Imperial fault, Eastern California Shear Zone (ECSZ), Garlock fault (GF), and Oak Ridge fault (ORF), and also appears to be high around the Los Angeles and Ventura basins. The maximum shear-strain rate of $\sim 7 \times 10^{-7}$ strain/yr across the creeping section of the SAF is the highest in the region; however the number is not indicative of elastic strain accumulation, but discontinuous offsets across the fault (Fig. 5). The second highest shear-strain rate of up to 4×10^{-7} strain/yr is across the Brawley Seismic Zone and the Imperial fault. Surface creeping was found across the Imperial fault (Lyons *et al.*, 2002). The Brawley Seismic Zone is geothermally active, and the seismogenic section of the fault is relatively shallow and may only be partially locked (Allam and Ben-Zion, 2012). The high strain rate across the Brawley Seismic Zone and the Imperial fault is therefore only partially elastic within the upper crust. The shear-strain rates are $\sim 3 \times 10^{-7}$ strain/yr across the Carrizo and Coachella sections of the SAF and the SJF and $\sim 2 \times 10^{-7}$ strain/yr across the Mojave and San Bernardino sections of the SAF. The north–south convergent strain rates are up to $1–2 \times 10^{-7}$ strain/yr across the ORF and Santa Monica fault and within the Los Angeles and Ventura basins. About 2×10^{-7} strain/yr is detected across the southern Mojave Shear Zone, which is perhaps partially due to postseismic seismic deformation of the 1992 M_w 7.3 Landers and 1999 M_w 7.1 Hector Mine earthquakes (Shen *et al.*, 2011). The shear-strain rate across the GF and the section of the ECSZ north of the GF are $0.5–1 \times 10^{-7}$ strain/yr. These results are consistent with previous findings by Jackson *et al.* (1997), Shen-Tu *et al.* (1999), and Ward (1998), but with better resolution. For example, strain concentrations around the southern SAF and the SJF can be distinctively identified, instead of merging together (Fig. 5a).

Some of the recent studies also achieved sharp lineation patterns along these faults by imposing *a priori* constraints

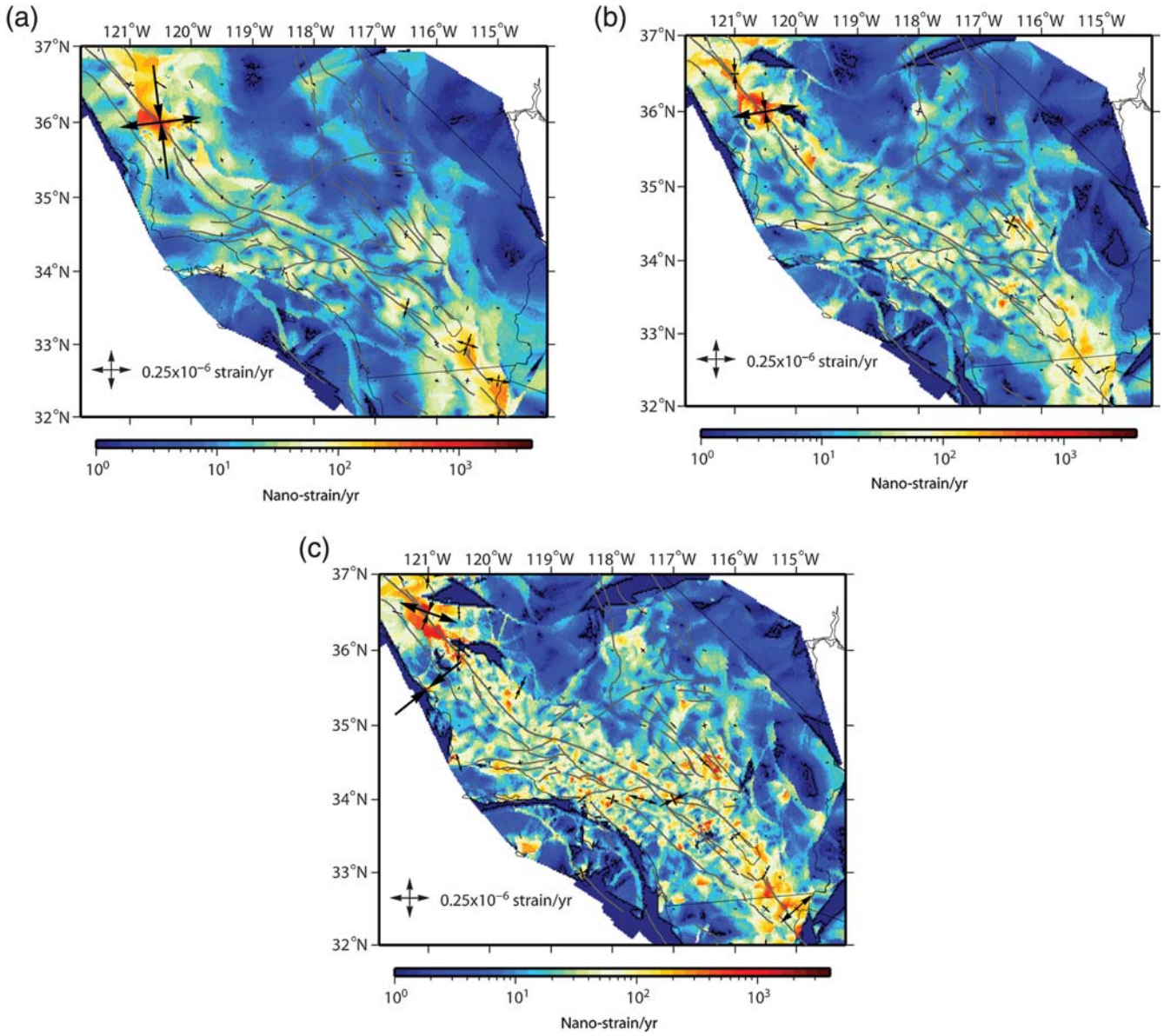

Figure 9. The differential strain-rate fields of Gaussian or Voronoi cell weighting and different net weighting threshold W_t. (a) $(W_t = 24) - (W_t = 48)$; (b) $(W_t = 12) - (W_t = 24)$; and (c) $(W_t = 6) - (W_t = 12)$. The background denotes the second invariant of differential strain rates and the arrow pairs are the differential principal strain rates, respectively.

such as wrench-style dislocation across the faults or alignment of maximum shear-strain orientation with the fault strike direction (e.g., Kreemer *et al.*, 2012, 2014). Such assumptions are effective in highlighting the strains across the faults for a region where tectonics is well understood, but may not always be valid in the real world. Our method does not require such knowledge.

Figure 10 shows the amplitudes and orientations of maximum strain rates (with Gaussian and Voronoi cell weighting, $W_t = 24$), and how that coincides with the strikes of major faults in southern California. This result also provides an independent validation check for the aforementioned assumption that the maximum shear strains are aligned with strike-slip fault orientations. From the figure, it can be seen that the strike directions of the dextral maximum shear coincides remarkably well with most of the northwest-striking strike-slip fault segments, such as the Carrizo and Coachella segments of the SAF, Imperial fault, and SJF. Even in the Big Bend of the SAF region, the strike direction of the dextral maximum shear aligns well with the Mojave segment of the SAF. The regions where the dextral maximum shear-strain rates deviate significantly from the local strike-slip fault orientations are at the San Bernardino, Mission Creek, and Tejon Pass segments of the SAF, and the Mojave Shear Zone, where the dextral maximum shear-strain rates orient clockwise relative to the local fault strike directions. The sinistral maximum shear-strain rates orient in general counterclockwise from the sinistral slip faults such as the GF and Big Pine fault (BPF). These results suggest

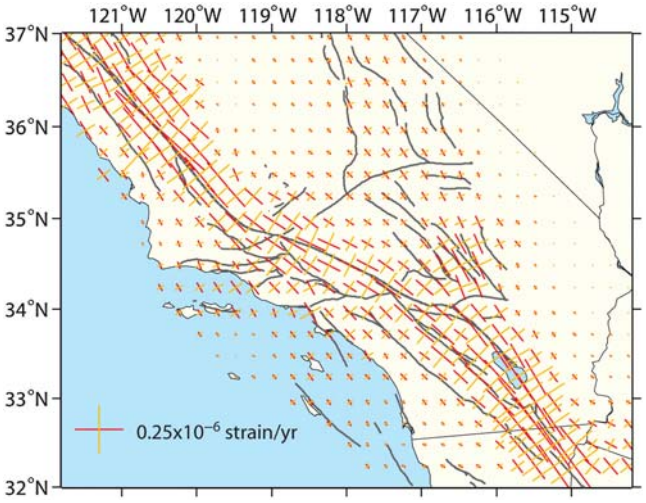

Figure 10. Maximum shear-strain rates. The red and orange bars show the amplitudes and orientations of the dextral and sinistral maximum shear-strain rates, respectively. CaSAF, Carrizo SAF; CoSAF, Coachella SAF; CrSAF, Creeping segment of SAF; MoSAF, Mojave SAF; TPSAF, Tejon Pass SAF; SBSAF, San Bernardino SAF; SJF, San Jacinto fault; BPF, Big Pine fault; GF, Garlock fault; MSZ, Mojave Shear Zone; ECSZ, East California Shear Zone; LAB, Los Angeles basin; VB, Ventura basin.

that the SAF, including the segment around the Big Bend, dictates the tectonic deformation field of southern California. Other faults such as the GF, the BPF, and the ones in the Mojave Shear Zone, play a secondary role in spreading the deformation field around the SAF, and their stress or strain state are significantly affected by the mechanical processes along the SAF.

The rotation rate pattern follows pretty much the shear-strain-rate pattern along the SAF and SJF (Fig. 5a,b). However, it shows some interesting features off the SAF system. About $1–2 \times 10^{-7}$ radian/yr clockwise rotation is found within the Mojave block. For a pure strike-slip dislocation it would produce equal amount of shear strain and rotation, but this rotation rate exceeds the shear-strain rate in the central and northern part of the block. The strain rates in the central and north part of the block are not affected by as much postseismic deformation as that in the southern block, thus this feature reveals present-day active clockwise rotation of the Mojave block. Minimum clockwise rotation rates are found around the GF and ORF, resulting from counter-clockwise rotations associated with the sinistral motion across the faults. Such local counter-clockwise rotations offset the regional clockwise rotation associated with the dextral motion across the plate boundary zone, resulting in local minimal rotation rates. This effect is particularly significant around the ORF, which shows $\sim 3 \times 10^{-8}$ radian/yr counterclockwise rotation.

Conclusions

In this article, we introduce a fully implemented method to optimally estimate strain field as a continuous function using discrete geodetic measurements. This method is robust because it does not rely on certain assumptions on data as do some other methods such as stationarity and isotropy. This method also balances between stability and resolution, relying on *in situ* data strength to determine the degree of smoothing to be imposed on the neighboring data.

Application of this method to the SCEC CMM4 velocity field provides the present-day strain-rate field in southern California. Our result shows that (1) distance-dependent weighting can be optimally achieved by employing either a Gaussian or quadratic decay function, with the former offering a slightly sharper result than the latter with a given range of data selection. (2) Spatially dependent weighting is important to improve the interpolation, and can be done by invoking either an azimuthal weighting or a Voronoi cell areal weighting function. Excluding the nonelastic strain along the creeping section of the SAF, the regional strain-rate field reveals that (1) the highest strain rate, up to 4×10^{-7} strain/yr is found across the Brawley Seismic Zone and the Imperial fault. (2) About $2–3 \times 10^{-7}$ strain/yr shear-strain rates are detected across the SAF from the Carrizo Plain to Coachella segment, the SJF and ORF, and the Mojave Shear Zone. (3) North–south convergence of up to 1.5×10^{-7} strain/yr is resolved within the Los Angeles and Ventura basins. (4) Orientations of the dextral maximum shear-strain rates coincide well with the strike directions of the SAF and the SJF, but other strike-slip faults off the SAF in the Transverse Ranges and Mojave Shear Zone region orient obliquely with respect to the maximum shear-strain-rate directions. These strain rates in alignment with the SAF orientation suggest that tectonic deformation field on and off the SAF in southern California is dominated by mechanical processes of the SAF.

Data and Resources

The Global Positioning System (GPS) velocity data are from the Southern California Earthquake Center (SCEC) Crustal Motion Map version 4.0 (CMM4) and can be found at http://scec.ess.ucla.edu/~zshen/cmm4/cmm4.html (last accessed February 2015). The computer code velocity interpolation for strain rate (VISR) for strain derivation and an example of its application to the SCEC CMM4 data can be found at http://scec.ess.ucla.edu/~zshen/visr/visr.html (last accessed February 2015). Materials of the strain derivation methods and results presented at the 2010 SCEC workshop were obtained from ftp://topex.ucsd.edu/pub/sandwell/strain/ (last accessed February 2015). Some plots were made using the Generic Mapping Tools version 4.2.1 (www.soest.hawaii.edu/gmt, last accessed February 2015; Wessel and Smith, 1998).

Acknowledgments

The authors thank Corne Kreemer, an anonymous reviewer, and Associate Editor Roland Burgmann for constructive comments. This research was partially supported by a China Earthquake Administration (CEA) Grant Number (201208006) for M. Wang and a Natural Science Foundation of China (NSFC) Grant Number (41090294) and a U.S. Geological Survey Grant Number (G11AP20044) for Z.-K. Shen. It was also supported by a National Science Foundation Inter-agency Research and Development (NSF I/RD) Grant Number (EAR-1323052) for Z.-K. Shen as a rotator pro-

gram director at NSF. Any opinions, findings, and conclusions or recommendations expressed in this article are those of the author(s) and do not necessarily reflect the views of the NSF and USGS. Southern California Earthquake Center Publication Number 2077.

References

Allam, A. A., and Y. Ben-Zion (2012). Seismic velocity structures in the southern California plate-boundary environment from double-difference tomography, *Geophys. J. Int.* **190,** 1181–1196, doi: 10.1111/j.1365-246X.2012.05544.x.

Brunner, F. K., R. Coleman, and B. Hirsch (1981). A comparison of computation methods for crustal strains from geodetic measurements, *Tectonophysics* **71,** 281–298.

El-Fiky, G. S., and T. Kato (1999). Continuous distribution of the horizontal strain in the Tohoku district, Japan, deduced from least squares prediction, *J. Geodyn.* **27,** 213–236.

El-Fiky, G. S., T. Kato, and Y. Fujii (1997). Distribution of vertical crustal movement rates in the Tohoku district, Japan, predicted by least-squares collocation, *J. Geodes.* **71,** 432–442.

Fortune, S. (1992). Voronoi diagrams and Delaunay triangulations, in *Computing in Euclidean Geometry*, Z.-Z. Du and F. K. Hwang (Editors), World Scientific Publishing Co., Singapore, 193–233.

Frank, F. C. (1966). Deduction of Earth strains from survey data, *Bull. Seismol. Soc. Am.* **56,** 35–42.

Haines, A. J., and W. E. Holt (1993). A procedure for obtaining the complete horizontal motions within zones of distributed deformation from the inversion of strain rate data, *J. Geophys. Res.* **98,** 12,057–12,082.

Hearn, E., K. Johnson, D. Sandwell, and W. Thatcher (2010). *SCEC UCERF Workshop Report*, http://www.scec.org/workshops/2010/gps-ucerf3/FinalReport_GPS-UCERF3Workshop.pdf (last accessed June 2015).

Holt, W. E., N. Chamot-Rooke, X. LePichon, A. J. Haines, B. Shen-Tu, and J. Ren (2000). Velocity field in Asia inferred from quaternary fault slip rates and global positioning system observations, *J. Geophys. Res.* **105,** 19,185–19,209.

Hsu, Y.-J., S.-B. Yu, M. Simons, L.-C. Kuo, and H.-Y. Chen (2009). Interseismic crustal deformation in the Taiwan plate boundary zone revealed by GPS observations, seismicity, and earthquake focal mechanisms, *Tectonophysics* **479,** 4–18.

Jackson, D. D., Z.-K. Shen, D. Potter, X. Ge, and L. Sung (1997). Earthquakes and strain in southern California, *Science* **277,** 1621–1622.

Jolivet, R., M. Simons, P. S. Agram, Z. Duputel, and Z.-K. Shen (2015). Aseismic slip and seismogenic coupling along the central San Andreas fault, *Geophys. Res. Lett.* **42,** no. 2, doi: 10.1002/2014GL062222.

Kreemer, C., G. Blewitt, and E. C. Klein (2014). A geodetic plate motion and global strain rate model, *Geochem. Geophys. Geosyst.* **15,** 3849–3889, doi: 10.1002/2014GC005407.

Kreemer, C., W. C. Hammond, G. Blewitt, A. A. Austin, and R. A. Bennett (2012). A geodetic strain rate model for the Pacific-North American plate boundary, western United States, *Nevada Bureau of Mines and Geology Map 178*, scale 1:1,500,000.

Kreemer, C., W. E. Holt, and A. J. Haines (2003). An integrated global model of present-day plate motions and plate boundary deformation, *Geophys. J. Int.* **154,** 8–34, doi: 10.1046/j.1365-246X.2003.01917.x.

Lyons, S. N., Y. Bock, and D. T. Sandwell (2002). Creep along the Imperial Fault, southern California, from GPS measurements, *J. Geophys. Res.* **107,** no. B10, 2249, doi: 10.1029/2001JB000763.

Matheron, G. (1970). Random functions and their application in geology, in *Geostatistics*, Plenum Press, New York, New York, 79–87.

Mitášová, H., and L. Mitáš (1993). Interpolation by regularized spline with tension: I. Theory and implementation, *Math. Geol.* **25,** 641–655.

Noda, A., and M. Matsu'ura (2010). Physics-based GPS data inversion to estimate three-dimensional elastic and inelastic strain fields, *Geophys. J. Int.* **182,** 513–530, doi: 10.1111/j.1365-246X.2010.04611.x.

Prescott, W. H. (1976). An extension of Frank's method for obtaining crustal shear strains from survey data, *Bull. Seismol. Soc. Am.* **66,** 1847–1853.

Sandwell, D. T. (1987). Biharmonic spline interpolation of GEOS-3 and SEASAT altimeter data, *Geophys. Res. Lett.* **14,** no. 2, 139–142.

Shen, Z.-K., D. Dong, T. Herring, K. Hudnut, D. Jackson, R. King, S. McClusky, and L. Sung (1997). Geodetic measurements of southern California crustal deformation, *Eos Trans. AGU* **78,** no. 43, 477–482.

Shen, Z.-K., D. D. Jackson, and B. X. Ge (1996). Crustal deformation across and beyond the Los Angeles basin from geodetic measurements, *J. Geophys. Res.* **101,** 27,957–27,980.

Shen, Z.-K., D. D. Jackson, and Y. Y. Kagan (2007). Implications of geodetic strain rate for future earthquakes, with a five-year forecast of *M* 5 earthquakes in southern California, *Seismol. Res. Lett.* **78,** no. 1, 117–120.

Shen, Z.-K., R. W. King, D. C. Agnew, M. Wang, T. A. Herring, D. Dong, and P. Fang (2011). A unified analysis of crustal motion in southern California, 1970–2004: The SCEC Crustal Motion Map, *J. Geophys. Res.* **116,** no. B11402, doi: 10.1029/2011JB008549.

Shen-Tu, B., W. E. Holt, and A. J. Haines (1999). Deformation kinematics in the western United States determined from Quaternary fault slip rates and recent geodetic data, *J. Geophys. Res.* **104,** no. B12, 28,927–28,955, doi: 10.1029/1999JB900293.

Srivastava, H., and E. Isaaks (1989). *An Introduction to Applied Geostatistics*, Oxford University Press, 561 pp.

Wackernagel, H. (1995). *Multivariate Geostatistics*, Springer, Berlin, Germany, 256 pp.

Ward, S. (1998). On the consistency of earthquake moment rates, geological fault data, and space geodetic strain: The United States, *Geophys. J. Int.* **134,** 172–186.

Wessel, P., and J. M. Becker (2008). Interpolation using a generalized Green's function for a spherical surface spline in tension, *Geophys. J. Int.* **174,** 21–28.

Wessel, P., and D. Bercovici (1998). Interpolation with splines in tension: A Green's function approach, *Math. Geol.* **30,** 77–93.

Wessel, P., and W. H. F. Smith (1998). New, improved version of generic mapping tools released, *Eos Trans. AGU* **79,** no. 47, 579–579, doi: 10.1029/98EO00426.

School of Earth and Space Science
Peking University
Beijing 100871, China
zshen@ucla.edu
(Z.-K.S.)

State Key Laboratory of Earthquake Dynamics
Institute of Geology
China Earthquake Administration
Beijing 100029, China
(M.W.)

U.S. Geological Survey Golden
Colorado Office
MS 966, Box 25046
Denver, Colorado 80225
(Y.Z.)

National Geomatics Center of China
28 Lianhuachi West Road
Haidian District
Beijing 100830, China
(F.W.)

Manuscript received 17 August 2014;
Published Online 14 July 2015;
Corrected Online 21 July 2015